EUROPEAN ORGANIZATION FOR NUCLEAR RESEARCH

CERN–PPE/94–131

4 August 1994

Measurement of the $\Gamma_{b\bar{b}}/\Gamma_{had}$ Branching Ratio of the Z by Double Hemisphere Tagging

DELPHI Collaboration

Abstract

Two measurements of $\Gamma_{b\bar{b}}/\Gamma_{had}$ are presented. Both measurements use 250000 Z decays taken with the DELPHI detector in 1991 and rely mainly on the precision of the microvertex detector. One tagging method is as simple as possible so that background rates can be reliably predicted by simulation. The other one uses a more involved tagging technique and reduces the dependence on simulation as much as possible. Combining both results, $\Gamma_{b\bar{b}}/\Gamma_{had}$ is found to be $0.2209 \pm 0.0041\,(stat.) \pm 0.0042\,(syst.) \pm 0.0018\,(\Gamma_{c\bar{c}})$.

(To be submitted to Zeit. f. Physik C)

P.Abreu[20], W.Adam[7], T.Adye[37], E.Agasi[30], I.Ajinenko[42], R.Aleksan[39], G.D.Alekseev[14], P.P.Allport[21], S.Almehed[23], F.M.L.Almeida[47], S.J.Alvsvaag[4], U.Amaldi[7], A.Andreazza[27], P.Antilogus[24], W-D.Apel[15], R.J.Apsimon[37], Y.Arnoud[39], B.Åsman[44], J-E.Augustin[18], A.Augustinus[30], P.Baillon[7], P.Bambade[18], F.Barao[20], R.Barate[12], G.Barbiellini[46], D.Y.Bardin[14], G.J.Barker[34], A.Baroncelli[40], O.Barring[7], J.A.Barrio[25], W.Bartl[50], M.J.Bates[37], M.Battaglia[13], M.Baubillier[22], J.Baudot[39], K-H.Becks[52], M.Begalli[36], P.Beilliere[6], Yu.Belokopytov[7], P.Beltran[9], A.C.Benvenuti[5], M.Berggren[41], D.Bertrand[2], F.Bianchi[45], M.Bigi[45], M.S.Bilenky[14], P.Billoir[22], J.Bjarne[23], D.Bloch[8], J.Blocki[51], S.Blyth[34], V.Bocci[38], P.N.Bogolubov[14], T.Bolognese[39], M.Bonesini[27], W.Bonivento[27], P.S.L.Booth[21], G.Borisov[42], C.Bosio[40], B.Bostjancic[43], S.Bosworth[34], O.Botner[48], B.Bouquet[18], C.Bourdarios[18], T.J.V.Bowcock[21], M.Bozzo[11], S.Braibant[2], P.Branchini[40], K.D.Brand[35], R.A.Brenner[13], H.Briand[22], C.Bricman[2], L.Brillault[22], R.C.A.Brown[7], P.Bruckman[16], J-M.Brunet[6], L.Bugge[32], T.Buran[32], A.Buys[7], J.A.M.A.Buytaert[7], M.Caccia[27], M.Calvi[27], A.J.Camacho Rozas[41], R.Campion[21], T.Camporesi[7], V.Canale[38], K.Cankocak[44], F.Cao[2], F.Carena[7], P.Carrilho[47], L.Carroll[21], R.Cases[49], C.Caso[11], M.V.Castillo Gimenez[49], A.Cattai[7], F.R.Cavallo[5], L.Cerrito[38], V.Chabaud[7], A.Chan[1], Ph.Charpentier[7], L.Chaussard[24], J.Chauveau[22], P.Checchia[35], G.A.Chelkov[14], P.Chliapnikov[42], V.Chorowicz[22], J.T.M.Chrin[49], V.Cindro[43], P.Collins[34], J.L.Contreras[18], R.Contri[11], E.Cortina[49], G.Cosme[18], F.Couchot[18], H.B.Crawley[1], D.Crennell[37], G.Crosetti[11], J.Cuevas Maestro[33], S.Czellar[13], E.Dahl-Jensen[28], J.Dahm[52], B.Dalmagne[18], M.Dam[32], G.Damgaard[28], E.Daubie[2], A.Daum[15], P.D.Dauncey[37], M.Davenport[7], J.Davies[21], W.Da Silva[22], C.Defoix[6], P.Delpierre[26], N.Demaria[34], A.De Angelis[7], H.De Boeck[2], W.De Boer[15], S.De Brabandere[2], C.De Clercq[2], M.D.M.De Fez Laso[49], C.De La Vaissiere[22], B.De Lotto[46], A.De Min[27], L.De Paula[47], C.De Saint-Jean[39], H.Dijkstra[7], L.Di Ciaccio[38], F.Djama[8], J.Dolbeau[6], M.Donszelmann[7], K.Doroba[51], M.Dracos[8], J.Drees[52], M.Dris[31], Y.Dufour[7], F.Dupont[12], D.Edsall[1], R.Ehret[15], T.Ekelof[48], G.Ekspong[44], M.Elsing[52], J-P.Engel[8], N.Ershaidat[22], M.Espirito Santo[20], D.Fassouliotis[31], M.Feindt[7], A.Fenyuk[42], A.Ferrer[49], T.A.Filippas[31], A.Firestone[1], H.Foeth[7], E.Fokitis[31], F.Fontanelli[11], F.Formenti[7], J-L.Fousset[26], B.Franek[37], P.Frenkiel[6], D.C.Fries[15], A.G.Frodesen[4], R.Fruhwirth[50], F.Fulda-Quenzer[18], H.Furstenau[7], J.Fuster[7], D.Gamba[45], M.Gandelman[17], C.Garcia[49], J.Garcia[41], C.Gaspar[7], U.Gasparini[35], Ph.Gavillet[7], E.N.Gazis[31], D.Gele[8], J-P.Gerber[8], P.Giacomelli[7], D.Gillespie[7], R.Gokieli[51], B.Golob[43], V.M.Golovatyuk[14], J.J.Gomez Y Cadenas[7], G.Gopal[37], L.Gorn[1], M.Gorski[51], V.Gracco[11], F.Grard[2], E.Graziani[40], G.Grosdidier[18], P.Gunnarsson[44], J.Guy[37], U.Haedinger[15], F.Hahn[52], M.Hahn[44], S.Hahn[52], S.Haider[30], Z.Hajduk[16], A.Hakansson[23], A.Hallgren[48], K.Hamacher[52], W.Hao[30], F.J.Harris[34], V.Hedberg[23], R.Henriques[20], J.J.Hernandez[49], J.A.Hernando[49], P.Herquet[2], H.Herr[7], T.L.Hessing[21], E.Higon[49], H.J.Hilke[7], T.S.Hill[1], S-O.Holmgren[44], P.J.Holt[34], D.Holthuizen[30], P.F.Honore[6], M.Houlden[21], J.Hrubec[50], K.Huet[2], K.Hultqvist[44], P.Ioannou[3], P-S.Iversen[4], J.N.Jackson[21], R.Jacobsson[44], P.Jalocha[16], G.Jarlskog[23], P.Jarry[39], B.Jean-Marie[18], E.K.Johansson[44], M.Jonker[7], L.Jonsson[23], P.Juillot[8], M.Kaiser[15], G.Kalmus[37], F.Kapusta[22], M.Karlsson[44], E.Karvelas[9], S.Katsanevas[3], E.C.Katsoufis[31], R.Keranen[7], B.A.Khomenko[14], N.N.Khovanski[14], B.King[21], N.J.Kjaer[28], H.Klein[7], A.Klovning[4], P.Kluit[30], A.Koch-Mehrin[52], J.H.Koehne[15], B.Koene[30], P.Kokkinias[9], M.Koratzinos[32], A.V.Korytov[14], V.Kostioukhine[42], C.Kourkoumelis[3], O.Kouznetsov[14], P.H.Kramer[52], M.Krammer[50], C.Kreuter[15], J.Krolikowski[51], I.Kronkvist[23], W.Krupinski[16], W.Kucewicz[16], K.Kulka[48], K.Kurvinen[13], C.Lacasta[49], I.Laktineh[24], C.Lambropoulos[9], J.W.Lamsa[1], L.Lanceri[46], P.Langefeld[52], V.Lapin[42], I.Last[21], J-P.Laugier[39], R.Lauhakangas[13], G.Leder[50], F.Ledroit[12], R.Leitner[29], Y.Lemoigne[39], J.Lemonne[2], G.Lenzen[52], V.Lepeltier[18], T.Lesiak[35], J.M.Levy[8], E.Lieb[52], D.Liko[50], R.Lindner[52], A.Lipniacka[18], I.Lippi[35], B.Loerstad[23], M.Lokajicek[10], J.G.Loken[34], A.Lopez-Fernandez[7], M.A.Lopez Aguera[41], M.Los[30], D.Loukas[9], J.J.Lozano[49], P.Lutz[39], L.Lyons[34], G.Maehlum[15], J.Maillard[6], A.Maio[20], A.Maltezos[9], J.Marco[41], B.Marechal[47], M.Margoni[35], J-C.Marin[7], C.Mariotti[40], A.Markou[9], T.Maron[52], S.Marti[49], C.Martinez-Rivero[41], F.Martinez-Vidal[49], F.Matorras[41], C.Matteuzzi[27], G.Matthiae[38], M.Mazzucato[35], M.Mc Cubbin[21], R.Mc Kay[1], R.Mc Nulty[21], J.Medbo[48], C.Meroni[27], W.T.Meyer[1], M.Michelotto[35], E.Migliore[45], I.Mikulec[50], L.Mirabito[24], W.A.Mitaroff[50], G.V.Mitselmakher[14], U.Mjoernmark[23], T.Moa[44], R.Moeller[28], K.Moenig[7], M.R.Monge[11], P.Morettini[11], H.Mueller[15], W.J.Murray[37], B.Muryn[16], G.Myatt[34], F.Naraghi[12], F.L.Navarria[5], P.Negri[27], S.Nemecek[10], W.Neumann[52], N.Neumeister[50], R.Nicolaidou[3], B.S.Nielsen[28], V.Nikolaenko[24], P.Niss[44], A.Nomerotski[35], A.Normand[34], V.Obraztsov[42], A.G.Olshevski[14], R.Orava[13], K.Osterberg[13], A.Ouraou[39], P.Paganini[18], M.Paganoni[27], R.Pain[22], H.Palka[16], Th.D.Papadopoulou[31], L.Pape[7], F.Parodi[11], A.Passeri[40], M.Pegoraro[35], J.Pennanen[13], L.Peralta[20], V.Perevozchikov[42], H.Pernegger[50], M.Pernicka[50], A.Perrotta[5], C.Petridou[46], A.Petrolini[11], H.T.Phillips[37], G.Piana[11], F.Pierre[39], M.Pimenta[20], S.Plaszczynski[18], O.Podobrin[15], M.E.Pol[17], G.Polok[16], P.Poropat[46], V.Pozdniakov[14], M.Prest[46], P.Privitera[38], A.Pullia[27], D.Radojicic[34], S.Ragazzi[27], H.Rahmani[31], J.Rames[10], P.N.Ratoff[19], A.L.Read[32], M.Reale[52], P.Rebecchi[18], N.G.Redaelli[27], M.Regler[50], D.Reid[7], P.B.Renton[34], L.K.Resvanis[3], F.Richard[18], J.Richardson[21], J.Ridky[10], G.Rinaudo[45], I.Ripp[39], A.Romero[45], I.Roncagliolo[11], P.Ronchese[35], V.Ronjin[42], L.Roos[12], E.I.Rosenberg[1], E.Rosso[7], P.Roudeau[18], T.Rovelli[5], W.Ruckstuhl[30], V.Ruhlmann-Kleider[39], A.Ruiz[41], H.Saarikko[13], Y.Sacquin[39], G.Sajot[12], J.Salt[49], J.Sanchez[25], M.Sannino[11], S.Schael[7], H.Schneider[15], M.A.E.Schyns[52], G.Sciolla[45], F.Scuri[46], A.M.Segar[34], A.Seitz[15], R.Sekulin[37], M.Sessa[46], R.Seufert[15], R.C.Shellard[36], I.Siccama[30], P.Siegrist[39], S.Simonetti[39], F.Simonetto[35], A.N.Sisakian[14], T.B.Skaali[32], G.Smadja[24], N.Smirnov[42], O.Smirnova[14], G.R.Smith[37], R.Sosnowski[51], D.Souza-Santos[36], T.Spassov[20], E.Spiriti[40], S.Squarcia[11], H.Staeck[52], C.Stanescu[40], S.Stapnes[32], I.Stavitski[35], G.Stavropoulos[9], K.Stepaniak[51], F.Stichelbaut[7], A.Stocchi[18], J.Strauss[50], J.Straver[7], R.Strub[8], B.Stugu[4], M.Szczekowski[51], M.Szeptycka[51], T.Tabarelli[27], O.Tchikilev[42], G.E.Theodosiou[9], Z.Thome[47], A.Tilquin[26], J.Timmermans[30], V.G.Timofeev[14], L.G.Tkatchev[14], T.Todorov[8], D.Z.Toet[30], A.Tomaradze[2], B.Tome[20], E.Torassa[45], L.Tortora[40], G.Transtromer[23], D.Treille[7], G.Tristram[6], C.Troncon[27], A.Tsirou[7], E.N.Tsyganov[14], M-L.Turluer[39], T.Tuuva[13], I.A.Tyapkin[22], M.Tyndel[37], S.Tzamarias[21], B.Ueberschaer[52], S.Ueberschaer[52], O.Ullaland[7], V.Uvarov[42], G.Valenti[5], E.Vallazza[7], J.A.Valls Ferrer[49], C.Vander Velde[2], G.W.Van Apeldoorn[30], P.Van Dam[30], M.Van Der Heijden[30], W.K.Van Doninck[2], J.Van Eldik[30], P.Vaz[7], G.Vegni[27], L.Ventura[35], W.Venus[37], F.Verbeure[2], M.Verlato[35], L.S.Vertogradov[14], D.Vilanova[39], P.Vincent[24], L.Vitale[46], E.Vlasov[42], A.S.Vodopyanov[14], M.Vollmer[52], M.Voutilainen[13], V.Vrba[10], H.Wahlen[52], C.Walck[44], F.Waldner[46], A.Wehr[52], M.Weierstall[52], P.Weilhammer[7], A.M.Wetherell[7], J.H.Wickens[2], M.Wielers[15], G.R.Wilkinson[34], W.S.C.Williams[34], M.Winter[8], M.Witek[7], G.Wormser[18], K.Woschnagg[48], K.Yip[34], O.Yushchenko[42], F.Zach[24], A.Zaitsev[42], A.Zalewska[16], P.Zalewski[51], D.Zavrtanik[43], E.Zevgolatakos[9], N.I.Zimin[14], M.Zito[39], D.Zontar[43], R.Zuberi[34], G.Zumerle[35]

---

[1] Ames Laboratory and Department of Physics, Iowa State University, Ames IA 50011, USA
[2] Physics Department, Univ. Instelling Antwerpen, Universiteitsplein 1, B-2610 Wilrijk, Belgium
and IIHE, ULB-VUB, Pleinlaan 2, B-1050 Brussels, Belgium
and Faculté des Sciences, Univ. de l'Etat Mons, Av. Maistriau 19, B-7000 Mons, Belgium
[3] Physics Laboratory, University of Athens, Solonos Str. 104, GR-10680 Athens, Greece
[4] Department of Physics, University of Bergen, Allégaten 55, N-5007 Bergen, Norway
[5] Dipartimento di Fisica, Università di Bologna and INFN, Via Irnerio 46, I-40126 Bologna, Italy
[6] Collège de France, Lab. de Physique Corpusculaire, IN2P3-CNRS, F-75231 Paris Cedex 05, France
[7] CERN, CH-1211 Geneva 23, Switzerland
[8] Centre de Recherche Nucléaire, IN2P3 - CNRS/ULP - BP20, F-67037 Strasbourg Cedex, France
[9] Institute of Nuclear Physics, N.C.S.R. Demokritos, P.O. Box 60228, GR-15310 Athens, Greece
[10] FZU, Inst. of Physics of the C.A.S. High Energy Physics Division, Na Slovance 2, 180 40, Praha 8, Czech Republic
[11] Dipartimento di Fisica, Università di Genova and INFN, Via Dodecaneso 33, I-16146 Genova, Italy
[12] Institut des Sciences Nucléaires, IN2P3-CNRS, Université de Grenoble 1, F-38026 Grenoble Cedex, France
[13] Research Institute for High Energy Physics, SEFT, P.O. Box 9, FIN-00014 Helsinki, Finland
[14] Joint Institute for Nuclear Research, Dubna, Head Post Office, P.O. Box 79, 101 000 Moscow, Russian Federation
[15] Institut für Experimentelle Kernphysik, Universität Karlsruhe, Postfach 6980, D-76128 Karlsruhe, Germany
[16] High Energy Physics Laboratory, Institute of Nuclear Physics, Ul. Kawiory 26a, PL-30055 Krakow 30, Poland
[17] Centro Brasileiro de Pesquisas Físicas, rua Xavier Sigaud 150, BR-22290 Rio de Janeiro, Brazil
[18] Université de Paris-Sud, Lab. de l'Accélérateur Linéaire, IN2P3-CNRS, Bat 200, F-91405 Orsay Cedex, France
[19] School of Physics and Materials, University of Lancaster, Lancaster LA1 4YB, UK
[20] LIP, IST, FCUL - Av. Elias Garcia, 14-1^o, P-1000 Lisboa Codex, Portugal
[21] Department of Physics, University of Liverpool, P.O. Box 147, Liverpool L69 3BX, UK
[22] LPNHE, IN2P3-CNRS, Universités Paris VI et VII, Tour 33 (RdC), 4 place Jussieu, F-75252 Paris Cedex 05, France
[23] Department of Physics, University of Lund, Sölvegatan 14, S-22363 Lund, Sweden
[24] Université Claude Bernard de Lyon, IPNL, IN2P3-CNRS, F-69622 Villeurbanne Cedex, France
[25] Universidad Complutense, Avda. Complutense s/n, E-28040 Madrid, Spain
[26] Univ. d'Aix - Marseille II - CPP, IN2P3-CNRS, F-13288 Marseille Cedex 09, France
[27] Dipartimento di Fisica, Università di Milano and INFN, Via Celoria 16, I-20133 Milan, Italy
[28] Niels Bohr Institute, Blegdamsvej 17, DK-2100 Copenhagen 0, Denmark
[29] NC, Nuclear Centre of MFF, Charles University, Areal MFF, V Holesovickach 2, 180 00, Praha 8, Czech Republic
[30] NIKHEF-H, Postbus 41882, NL-1009 DB Amsterdam, The Netherlands
[31] National Technical University, Physics Department, Zografou Campus, GR-15773 Athens, Greece
[32] Physics Department, University of Oslo, Blindern, N-1000 Oslo 3, Norway
[33] Dpto. Fisica, Univ. Oviedo, C/P. Pérez Casas, S/N-33006 Oviedo, Spain
[34] Department of Physics, University of Oxford, Keble Road, Oxford OX1 3RH, UK
[35] Dipartimento di Fisica, Università di Padova and INFN, Via Marzolo 8, I-35131 Padua, Italy
[36] Depto. de Fisica, Pontificia Univ. Católica, C.P. 38071 RJ-22453 Rio de Janeiro, Brazil
[37] Rutherford Appleton Laboratory, Chilton, Didcot OX11 OQX, UK
[38] Dipartimento di Fisica, Università di Roma II and INFN, Tor Vergata, I-00173 Rome, Italy
[39] Centre d'Etude de Saclay, DSM/DAPNIA, F-91191 Gif-sur-Yvette Cedex, France
[40] Istituto Superiore di Sanità, Ist. Naz. di Fisica Nucl. (INFN), Viale Regina Elena 299, I-00161 Rome, Italy
[41] C.E.A.F.M., C.S.I.C. - Univ. Cantabria, Avda. los Castros, S/N-39006 Santander, Spain, (CICYT-AEN93-0832)
[42] Inst. for High Energy Physics, Serpukov P.O. Box 35, Protvino, (Moscow Region), Russian Federation
[43] J. Stefan Institute and Department of Physics, University of Ljubljana, Jamova 39, SI-61000 Ljubljana, Slovenia
[44] Fysikum, Stockholm University, Box 6730, S-113 85 Stockholm, Sweden
[45] Dipartimento di Fisica Sperimentale, Università di Torino and INFN, Via P. Giuria 1, I-10125 Turin, Italy
[46] Dipartimento di Fisica, Università di Trieste and INFN, Via A. Valerio 2, I-34127 Trieste, Italy
and Istituto di Fisica, Università di Udine, I-33100 Udine, Italy
[47] Univ. Federal do Rio de Janeiro, C.P. 68528 Cidade Univ., Ilha do Fundão BR-21945-970 Rio de Janeiro, Brazil
[48] Department of Radiation Sciences, University of Uppsala, P.O. Box 535, S-751 21 Uppsala, Sweden
[49] IFIC, Valencia-CSIC, and D.F.A.M.N., U. de Valencia, Avda. Dr. Moliner 50, E-46100 Burjassot (Valencia), Spain
[50] Institut für Hochenergiephysik, Österr. Akad. d. Wissensch., Nikolsdorfergasse 18, A-1050 Vienna, Austria
[51] Inst. Nuclear Studies and University of Warsaw, Ul. Hoza 69, PL-00681 Warsaw, Poland
[52] Fachbereich Physik, University of Wuppertal, Postfach 100 127, D-42097 Wuppertal 1, Germany

1 Introduction

The ratio of the b quark partial width of the Z to its hadronic width is a particularly interesting quantity in the Standard Model. The propagator corrections that are measured with great precision elsewhere [1] largely cancel and only corrections to the $Zb\bar{b}$ vertex remain [2]. With a precise measurement of $R_b = \Gamma_{b\bar{b}}/\Gamma_{had}$ the top quark mass can be predicted essentially without residual model dependence.

In this paper we present two measurements with the DELPHI detector at LEP using about 250000 hadronic Z decays taken in 1991.

Both measurements take advantage of the DELPHI microvertex detector which allows a highly efficient separation of b and light quark events. The fraction of b events and their tagging efficiency are measured in both cases simultaneously by comparing the numbers of single and double hemisphere tagged events.

The first method, which is similar to an analysis published by the ALEPH collaboration [3], uses only the significance of the impact parameters of the tracks. Since this method is rather simple, the background from light quarks can be estimated reliably from simulation.

The second method is constructed to have reduced dependence on simulation. As explained later this needs an extremely pure b sample in the limit of very stringent cuts. For this reason a more elaborate procedure combining event shape and microvertex variables in a multivariate analysis is used.

The outline of this paper is as follows. After a brief description of the DELPHI detector and the charged particle and event selection, the main features of the two analyses are given. This is followed by a section explaining the combination of the two results and by our conclusions.

2 Charged Particle and Event Selection

The DELPHI detector has been described in detail elsewhere [4]. Therefore we shall mention here only the main features of the vertex detector (VD) which is essential to our analysis.

The vertex detector in the 1991 configuration consisted of 3 concentric shells of silicon strip detectors at radii of 6.5, 9 and 11 cm. It covered the central region over a length of 24 cm and defined an angular acceptance of $27^0 - 153^0$, $37^0 - 143^0$ and $42^0 - 138^0$ for hits in one, two or three layers. Each layer was composed of 24 modules with about 10% overlap in azimuth and each module consisted of 4 plaquettes along the beam direction. The intrinsic $R\phi$ resolution per layer, including alignment errors, has been evaluated to be 8μm.

The charged particle and event selection were slightly different for the details of the two analyses, however the main features are the same. The selection of charged particles is similar to [5]. For the measurement of impact parameter related variables, particles were only used if they had at least two associated hits in the VD. Neutral showers in the electromagnetic calorimeters were included in addition to charged particles to define hadronic Z decays and for the measurement of event shape variables. To select hadronic Z decays a minimum number of 5(6) charged particles and 10(20) GeV of seen energy were required in the first (second) analysis. According to simulation estimates, this criterion selects around 95 % of hadronic events with estimated contamination from decays $Z \rightarrow \tau^+\tau^-$ less than 0.1 % and negligible contamination of other processes (beam-gas, two photon events, other leptonic decays of Z, etc.) [5]. To ensure that most particles were contained in the VD acceptance it was also required that the absolute value of cosine of the polar angle of the thrust axis, $\cos(\Theta_{thr})$, was smaller than 0.75.

The JETSET 7.3 model [6] was used to generate events. The response of the DELPHI detector to the generated events was simulated using DELSIM [7]. A sample of 450000 simulated hadronic events was used.

3 Significance Analysis

This method is based on the fact that the b and $\bar{b}$ quarks from Z decays (and the corresponding heavy hadrons) are normally produced in opposite directions. On dividing such an event into 2 hemispheres (e.g. by the plane perpendicular to the thrust axis), each will, in general, contain one b hadron.

If with some tag a pure b flavour sample can be selected in one hemisphere, it is possible to find the efficiency of this selection and the fraction of $b\bar{b}$ events in the initial sample in a model-independent way by comparing the number of selected single hemispheres with the number of events in which both hemispheres are selected.

In practice the situation becomes more difficult because the background from the other flavours cannot be fully suppressed and thus should be subtracted properly. Additional problems arise from the fact that the hemispheres are not absolutely independent and the tag in one hemisphere biases the efficiency in the other, though this bias is small.

These statements may be expressed in the following form. If with some tag the efficiencies to select different flavours in one hemisphere are ϵ_b, ϵ_c and ϵ_q (where q stands for (uds) quarks, which are not separated) and the efficiencies to select events in which both hemispheres are tagged are ϵ'_b, ϵ'_c and ϵ'_q, one can write:

$$\begin{aligned} R_H &= R_b \cdot \epsilon_b + R_c \cdot \epsilon_c + (1 - R_b - R_c) \cdot \epsilon_q && (1) \\ R_E &= R_b \cdot \epsilon'_b + R_c \cdot \epsilon'_c + (1 - R_b - R_c) \cdot \epsilon'_q \\ &= R_b \cdot \{\epsilon_b^2 + \rho_b \cdot (\epsilon_b - \epsilon_b^2)\} + R_c \cdot \epsilon_c^2 + (1 - R_b - R_c) \cdot \epsilon_q^2. && (2) \end{aligned}$$

In these equations R_H is the fraction of tagged hemispheres, R_E the fraction of events in which both hemispheres are tagged and R_b and R_c the fractions of $Z \to b\bar{b}$ and $Z \to c\bar{c}$ events respectively in the initial hadronic sample. It is supposed that hadronic decays of the Z consist of $b\bar{b}$, $c\bar{c}$ and light quark final states, so that the fraction of the light quarks may be written as $R_q \equiv (1 - R_b - R_c)$. The event efficiency for the b flavour, ϵ'_b, is expressed as $\epsilon'_b = \epsilon_b^2 + \rho_b \cdot (\epsilon_b - \epsilon_b^2)$, which takes into account the correlation between hemispheres ρ_b. This form comes from the definition of the correlation coefficient $\rho = \frac{<(x-\mu_x)\cdot(y-\mu_y)>}{\sigma_x \cdot \sigma_y}$, which in this case leads to $\rho_b = \frac{\epsilon'_b - \epsilon_b^2}{\epsilon_b \cdot (1-\epsilon_b)}$. For c and uds flavours the tag efficiencies ϵ_c and ϵ_q are small enough (see eqns. 7 and 8 below) that the corresponding correlations do not influence R_b and ϵ_b and thus are not included in the equations above.

From eqns. 1 and 2 the fraction (R_b) and tagging efficiency (ϵ_b) can be extracted, provided the values ϵ_c, ϵ_q, ρ_b and R_c are known. The value of R_c can be taken from the world average results [1], while ϵ_c, ϵ_q, ρ_b are extracted from the simulation. If the b purity of the tagged sample is high, the dependence on simulation is small and may be included in the systematic uncertainties. For the correct assignment of the errors to the measured values of R_b and ϵ_b, the correlation of the variables R_H and R_E, which are not independent, has been taken into account.

3.1 The Tagging Technique

For the tagging of b flavour in hadronic decays of Z we use the probability method proposed originally by ALEPH [3]. It is based on the fact that, because of the non-zero lifetime of hadrons with heavy flavour content, particle tracks from decays of such hadrons have large positive [†] impact parameter with respect to the primary vertex while tracks from the primary vertex have impact parameters which are smaller in absolute value and may be either positive or negative with the same frequency.

For the reconstruction of the primary vertex and in the following analysis, at least 3 tracks with more than one associated hit in the vertex detector were required. The primary vertex was reconstructed in every event using beam spot information as a constraint. The full width at the half height of the primary vertex reconstruction in simulated events is around 50 μm for light quark events and 85 μm for the b quark events. The poorer resolution for the events with a b quark is mainly due to the smaller multiplicity of primary particles and due to the particles from the secondary decays which cannot be completely removed from the fit of the primary vertex.

The negative significance distribution, where the significance is defined as the impact parameter divided by its error, reflects mainly the detector resolution and is used to build the probability function $P(S_0)$, which is by definition the probability for particles from the primary vertex to have an absolute significance S_0 or greater. Mathematically this function is obtained for negative values of significance by integration of the distribution over the range below S_0, and assuming that for positive significance $P(S_0)$ should be the same:

$$P(S_0) = \begin{cases} \int_{S<S_0} f(S)dS & \text{if } S_0 < 0 \\ P(-S_0) & \text{if } S_0 > 0, \end{cases} \tag{3}$$

where $f(S)$ is the probability density function of the significance distribution. Particles from the decays of b hadrons which have the wrong sign assignment of the impact parameters are suppressed from the construction of $f(S)$ by requiring those events to pass an anti b cut $P_E^+ > 0.1$. The definition of the variable P_E^+ will be given later. Here we just note that this cut reduces the fraction of b events in the simulated sample to 6.5 %.

By construction, a flat distribution of $P(S_0)$ is expected for particles from the primary vertex, while for particles from the secondary vertices the distribution peaks at low probabilities.

Using the probability function, which is calculated separately for tracks with 2 VD hits and more than 2 VD hits, the probabilities for all particles in the event can be computed from their values of significance. After that, for any group of N particles (which may be particles from the total event or from one hemisphere) the N particle probability is defined as:

$$P_N \equiv \Pi \cdot \sum_{j=0}^{N-1} (-ln\Pi)^j/j!, \text{ where } \Pi \equiv \prod_{i=1}^{N} P(S_i). \tag{4}$$

This variable gives the probability for such a group of N particles with the observed values of significance to all be from the primary vertex. A group of particles from the primary vertex should have a flat distribution of P_N, provided the significances of these particles are uncorrelated. If the group includes particles from secondary vertices, the distribution has a peak at low values of P_N. This is illustrated in fig. 1, where the distributions of P_E^+ for different flavours are shown. P_E^+ is computed using eqn. 4 for all particles of the event with positive significance. The distribution of P_E^+ for light quarks is approximately flat, while for b quarks it has a sharp peak at zero.

[†] The sign of the impact parameter is defined with respect to the thrust axis. It is defined to be positive if the thrust axis is crossed in the direction of the track.

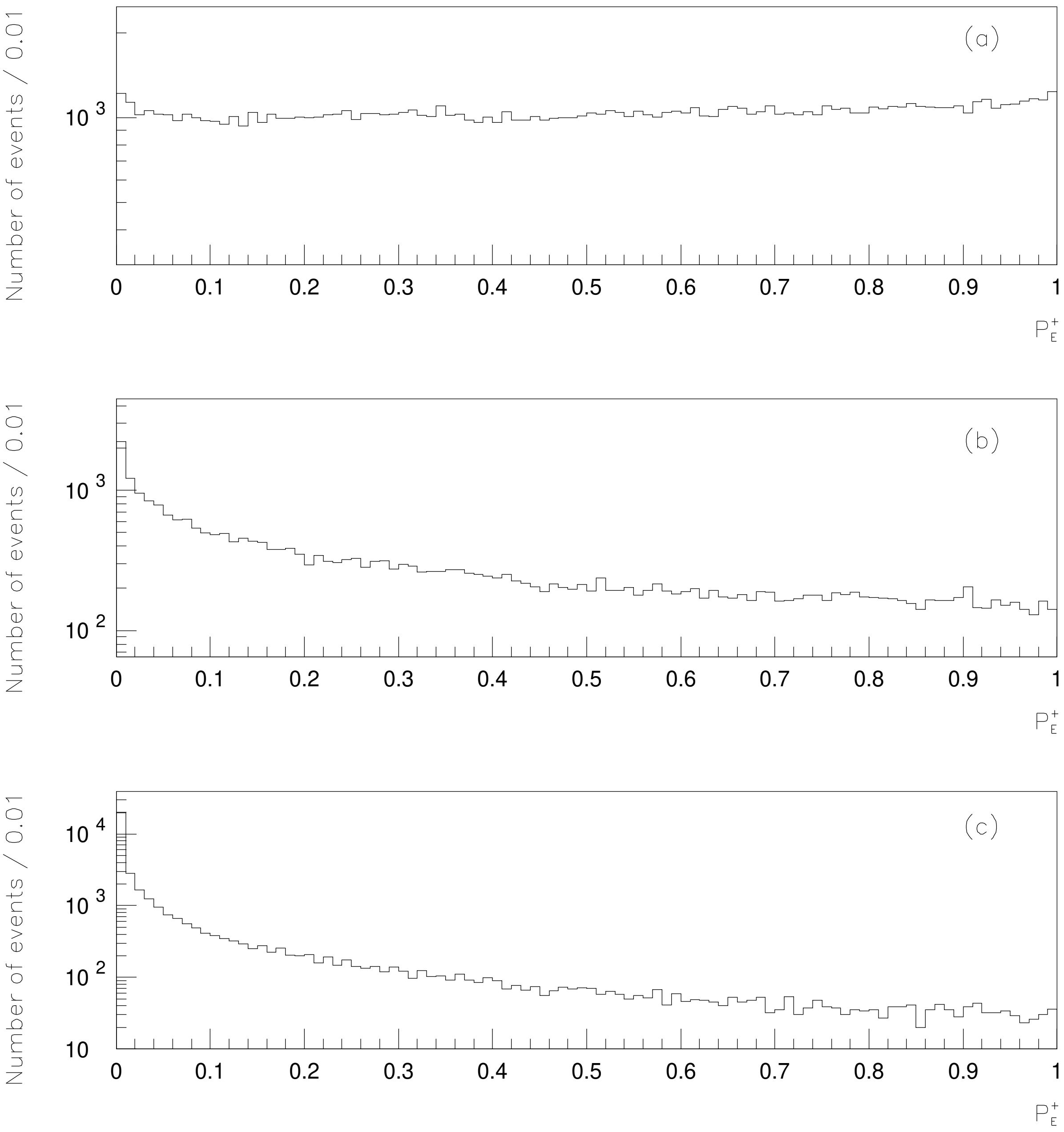

Figure 1: Distribution of event simulated probability P_E^+ for particles with positive impact parameters, for light quark events (a), charm quark events (b) and b-quark events(c).

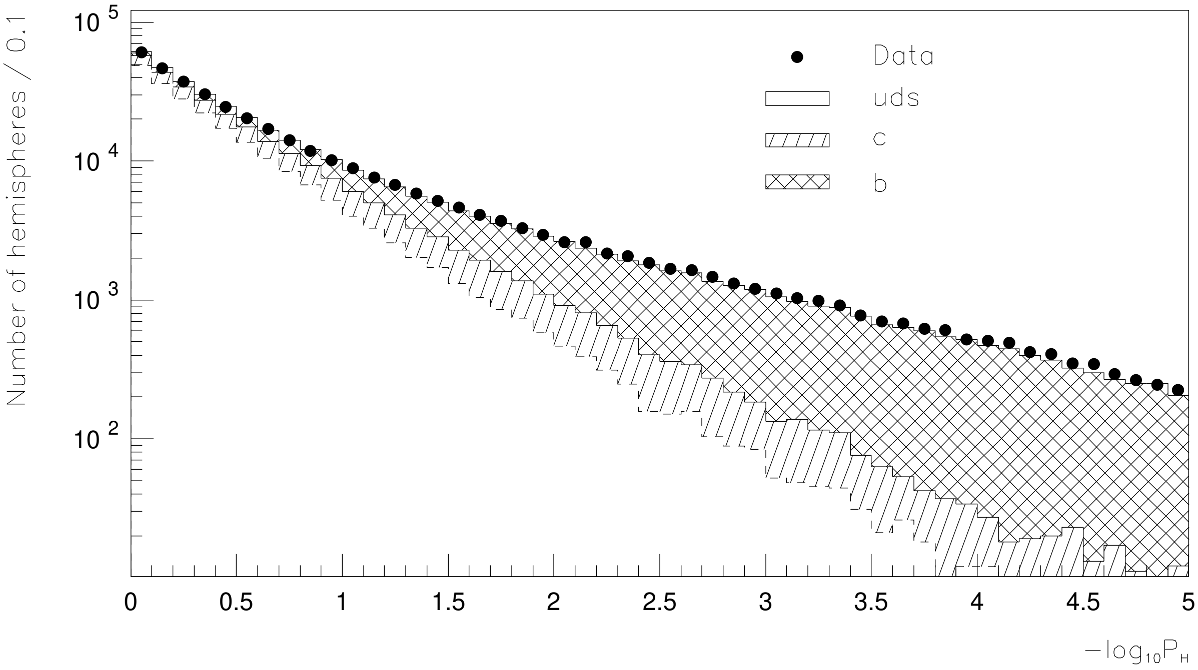

Figure 2: Distribution of $-\log_{10}(P_H)$ for data and different flavour contributions from the simulation.

The variable P_E^+ with the cut $P_E^+ > 0.1$ was used to obtain a sample of events with few b quarks, which is needed to construct an unbiased resolution curve. Since for the computation of P_E^+ the resolution curve is needed, its construction was done iteratively. The resolution curve obtained at the first step was used to calculate P_E^+ and this probability was used to select the new sample of events for construction of the resolution. Since the influence of events with b quarks on the resolution is small, the convergence of this procedure is very fast and after the second iteration a steady curve was obtained.

For the hemisphere tag another tagging variable, P_H, was used. P_H is defined as the probability, computed using eqn. 4, for all particles in one hemisphere, regardless of the sign of the impact parameter. It was found that this tagging variable gives almost the same efficiency for a given purity as the probability computed with only tracks of positive significance (P_H^+), but P_H^+ produces an additional correlation between hemispheres, because for the definition of the sign of impact parameter the common thrust axis was used. A cut on the impact parameter value of $|\delta| < 1.5$ mm was applied to reduce the background from K^0 and hyperon decays. Figure 2 shows the distribution of $-\log_{10}(P_H)$ in data and different flavour distributions obtained from the simulation. The cut $P_H < 0.00316$ ($-\log_{10}(P_H) > 2.5$), which is used for the measurement of R_b gives 89% purity of the tagged sample with a selection efficiency for hemispheres with b flavour of 23%, as estimated by the simulation.

3.2 Determination of the Resolution Function

The resolution function plays a crucial role for this method of tagging and to correctly interpret the values extracted from the simulation. In this analysis the resolution function was determined using the data only and the simulated events were forced to have the same distribution as the data. This was achieved in the following way:

- An analytical parameterisation was found which describes the negative significance distribution with reasonable accuracy. It was checked not only for the spectrum integrated over all particles, but also for subsamples with different momenta. All coefficients for it were extracted directly from a fit to the data.
- The errors both for data and simulated particles were assigned in the same way depending on the particle track fit parameters.
- The simulated particles were smeared around their "true" position (i.e. around the generated position of the parent vertex) according to the parameterisation obtained.

This procedure should give the same distributions of significance for data and simulation, provided the distributions of the track parameters (momentum, polar angle etc...) are the same.

In this analysis the resolution function was parameterised by the sum of Gaussians:

$$f(\delta_i) = \sum_{\alpha=1}^{n} \frac{C_\alpha}{\sqrt{2\pi}\,\sigma_{i\alpha}} \exp\left(-\frac{\delta_i^2}{2\sigma_{i\alpha}^2}\right). \tag{5}$$

In eqn. 5, δ_i is the impact parameter of the track, while variables $\sigma_{i\alpha}$ depend on the individual parameters of the track. The values C_α are constrained by the condition: $\sum_{\alpha=1}^{n} C_\alpha = 1$. The number of Gaussians used for the description of resolution, n, was 4.

The values of $\sigma_{i\alpha}$ were parameterised in the following way:

$$\begin{aligned} \sigma_{i1}^2 &= a^2 + \left(\frac{b}{p\sin^{3/2}(\Theta)}\right)^2 \\ \sigma_{i\alpha} &= k_\alpha \cdot \sigma_{i1}, \text{ for } \alpha > 1. \end{aligned} \tag{6}$$

In eqn. 6, Θ is the polar angle of the particle and p is the magnitude of its momentum. The expression for σ_{i1} has a physical motivation and has already been used in some previous analyses (see for example [8]). The first part (a^2) reflects the contribution of the intrinsic measurement resolution and the second part (proportional to b^2) gives the contribution of the multiple scattering. The expression for $\sigma_{i\alpha}$ ($\alpha > 1$) in the form of eqn. 6, along with the whole expression for the resolution function in eqn. 5, is a model which is found to give the best description of the data.

A comparison of the data and simulation significance distributions obtained by this technique is shown in fig. 3. Good agreement between data and simulation was obtained over practically the whole range of negative significance values.

3.3 Estimates of Efficiencies and Correlations

For the measurement of $\Gamma_{b\bar{b}}$, a cut $-\log_{10}(P_H) > 2.5$ was used. The values of ϵ_c, ϵ_q, ρ_b with this cut were extracted from Monte Carlo simulation and the possible sources of uncertainty were included as systematic errors.

The value of ϵ_q was found to be:

$$\epsilon_q = (0.419 \pm 0.010(stat.) \pm 0.038(syst.)) \cdot 10^{-2}. \tag{7}$$

The first error in eqn. 7 comes from limited statistics of simulation; the second is systematic. The different sources of systematic error are given in table 1. The systematic error due to uncertainties in the resolution function was estimated by varying the values

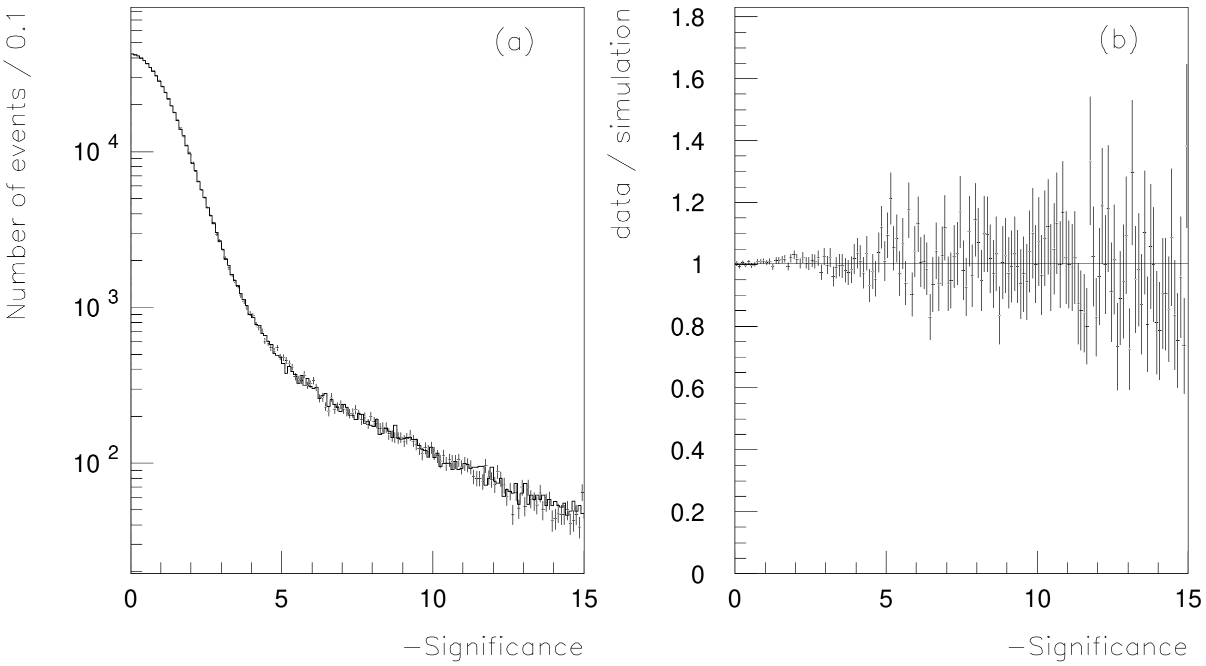

Figure 3: (a): Negative significance distribution for data (points with errors) and for simulation (histogram). (b) The ratio of negative significance distributions of data and simulation for tracks with negative impact parameters.

of the parameters used to describe the resolution within the errors obtained from the fit of the resolution function.

Long-lived particles (K^0, Λ) and secondary interactions (including conversions of $\gamma \to e^+e^-$) are two of the main sources of light quark background, responsible for about 40% of the total number of tagged light quark events, because they produce tracks with large impact parameters. The systematic error from these sources was obtained by allowing 20% variations in the production rate of these long-lived particles and secondary interactions (this number was obtained from the direct comparison of data and simulation).

The uncertainty from the difference in VD efficiencies between data and simulation was also included in the systematic error, though it is rather small.

Source of systematics	$\Delta\epsilon_q \times 10^4$
Resolution function	1.74
K^0, Hyperons, Secondary interactions	3.40
VD efficiency	0.30
Total	3.83

Table 1: Systematic errors of light quark efficiency ϵ_q

The efficiency to tag $Z \to c\bar{c}$ was found to be:

$$\epsilon_c = (2.16 \pm 0.04(stat.) \pm 0.15(syst.)) \cdot 10^{-2}. \quad (8)$$

The sources of systematic error are listed in table 2. The resolution function contribution was estimated as for the light quark background. The efficiency for tagging c quarks depends on the relative production rate of $D^{\pm}$ and D^0 because the lifetimes of these two mesons differ. The relative production rate in e^+e^- collisions was taken from data with $\sqrt{s}$ below the $b\bar{b}$ threshold [9], which excludes any contamination of b flavour, and was varied by 20%. The part of the systematic error which comes from the charm hadron lifetime uncertainties was obtained by varying them within the errors of reference [9]. To estimate the uncertainty due to charm decay multiplicity, the values and errors of the average charge multiplicity for different mesons were taken from experimental measurements [10]. The uncertainty due to the fragmentation function is relatively small and was estimated by varying the mean energy of charmed mesons within error limits from reference [11].

Source of systematics	$\Delta\epsilon_c \times 10^4$
Resolution function	7.2
$D^{\pm}/D^0$ production rate	8.4
D lifetime	7.0
Charm decay Multiplicity	6.5
Fragmentation	2.5
Total	14.8

Table 2: Systematic errors of charm quark efficiency ϵ_c

The correlation between hemispheres occurs due to polar angle acceptance, the fact that the beamspot constraint is common for both hemispheres, the common primary vertex which was not so well reconstructed for events with long-lived b hadrons and hard gluon emission in Z decay which results in many-jet events and may boost b hadrons into the same hemisphere.

The value of ρ_b together with its systematic uncertainties was again determined from the simulation to be:

$$\rho_b = (-0.13 \pm 0.37(stat.) \pm 0.18(syst.)) \cdot 10^{-2} \tag{9}$$

As one can see, the statistical error dominates in the determination of ρ_b. The systematic error includes the influence of the resolution function, the difference in the VD efficiency between data and simulation, a 10% change in the beamspot size (which corresponds to its stability and the accuracy of its determination) and a 6% variation of the errors of the primary vertex position (which corresponds to the maximal difference between data and simulation in the accuracy of primary vertex reconstruction for samples with different fractions of b events). The change of the lifetime of b hadrons may change the value of the correlation between hemispheres due to poorer primary vertex reconstruction so the systematic error also includes a contribution from varying the mean b hadron lifetime about the current world average value ($\tau_b = 1.521 \pm 0.034$ [12]). The systematic error from hard gluon emission, which may boost the two b hadrons into the same hemisphere, is estimated to be 20% of the effect in the simulation. This number is deduced from the uncertainty in α_s and from the difference in the prediction of the JETSET parton shower and matrix element models [6]. In addition to these sources the cut on the thrust axis direction – $|\cos\Theta_{thr}|$ – was varied from 0.65 to 0.85. With this variation the correlation factor ρ_b did change from -0.4 to 2.4 % but the variation of R_b was small (0.0007) and consistent with statistical fluctuations.

Table 3 shows the influence of the different sources of systematic error in the evaluation of ρ_b.

Source of systematics	$\Delta\rho_b \times 10^4$
Resolution function	10.3
Beam-spot size	9.5
Vertex-error estimate	8.7
VD efficiency	2.4
b-lifetime	7.0
Hard gluon emission	1.3
total	18.1

Table 3: Systematic errors of correlation factor ρ_b

3.4 Results

In total 176469 events within the acceptance of vertex detector were selected. In this sample 20677 hemispheres satisfy to the condition $-\log_{10}(P_H) > 2.5$ and in 2178 events both hemispheres have $-\log_{10}(P_H) > 2.5$. The only remaining unknown parameter for the measurement of R_b is R_c. This was taken from the value averaged over all LEP experiments [1]: $R_c = 0.171 \pm 0.014$. After the substitution of all values of efficiencies and correlation in eqns. 1 and 2 the following results were obtained:

$$\begin{aligned} \epsilon_b &= 0.2354 \pm 0.0043(stat.) \pm 0.0036(syst.) \\ R_b &= 0.2201 \pm 0.0040(stat.) \pm 0.0044(syst.) \pm 0.0019(\Gamma_{c\bar{c}}\ syst.). \end{aligned} \tag{10}$$

In eqn. 10 the systematic error coming from the value of $\Gamma_{c\bar{c}}$ is separated from all other sources. A change in the value of R_c would change R_b by $-0.14 \times (R_c - 0.171)$.

The list of systematic uncertainties is given in table 6. It includes not only the errors discussed above from light and charm quark efficiencies and the correlation factor, but also the error due to a small bias towards $b\bar{b}$ events in the selection of hadronic Z decays.

The results in eqn. 10 were obtained for the probability cut $-\log_{10}(P_H) > 2.5$ which was selected to minimize the total error of R_b. The dependence of different error sources on the probability cut is shown in fig. 4. Figure 5 shows the variation of R_b when changing the tagging cut. As one can see, there is no systematic dependence of the result on the value of the cut, but with variation of the cut the background content changes from 45% to 4% and the correlation factor changes from $+1.5\%$ to -0.5%. We consider this a rigorous test of the procedure for the evaluation of efficiencies and correlations.

In the significance distribution there is an unavoidable contribution from the particles from the decays of b hadrons which changes the resolution curve and hence may change the final result. To check the influence of this effect on R_b, the cut on P_E^+, which was used to select the sample of events with reduced contents of b hadrons, was varied from 0.05 to 0.50 and the analysis was repeated with the resolution functions determined with the different cuts on P_E^+. The variation of the cuts changes the b hadron content in the sample of events used for calibration from 12% to 3.5%, but the variation of R_b is small

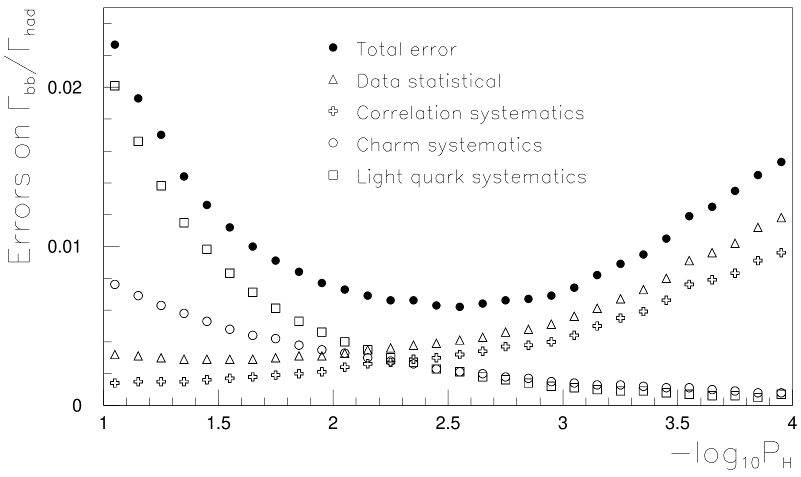

Figure 4: Errors of the measurement of $\Gamma_{b\bar{b}}\ /\Gamma_{had}$ as a function of the cut on $-\log_{10} P_H$.

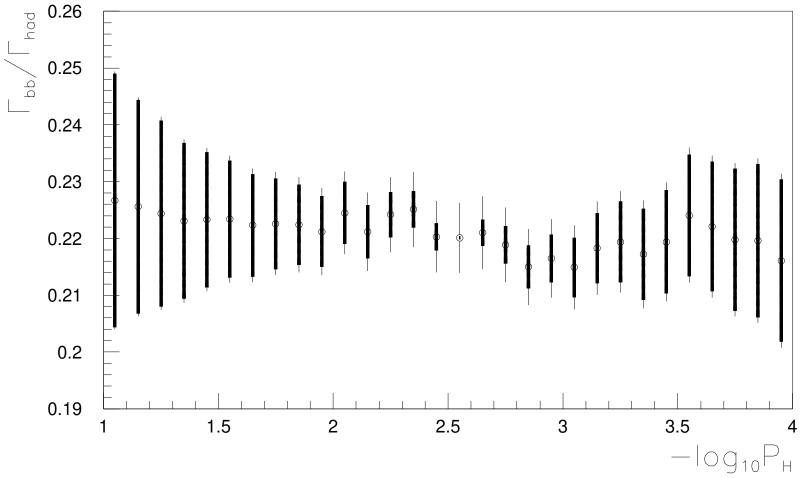

Figure 5: The value of $\Gamma_{b\bar{b}}\ /\Gamma_{had}$ as a function of the cut on $-\log_{10} P_H$. Both the total errors (narrow bars) and uncorrelated ones relative to the cut $-\log_{10} P_H > 2.5$ (wider bars) are shown.

(around 0.0013) and well within the expected uncertainty coming from the variation of the parameters of the resolution function.

In 1991 DELPHI took data at 7 different centre-of-mass energies around the Z peak. The difference between the value of R_b for different energies of the colliding beams and its value at the Z peak (91.2 GeV) has also been measured. This difference is not sensitive to any of the systematic effects mentioned above and the precision of the estimate depends only on the available statistics. The small changes in efficiencies for different centre-of-mass energies were taken from the simulation. The results obtained are shown in fig. 6 and in table 4. The theoretical expectation of ΔR_b was calculated using the program ZFITTER [13]. The results are consistent with the Standard Model prediction.

Energy (GeV)	88.5	89.5	90.2	92.1	93.1	93.7
$R_b(E) - R_b(91.2 \text{ GeV}) \times 10^2$	-2.69	0.31	-0.62	-0.17	-0.37	-0.78
Error ($\times 10^2$)	1.33	1.33	0.81	0.60	0.93	0.97

Table 4: The difference $R_b(E) - R_b(91.2 \text{ GeV})$ for the significance analysis

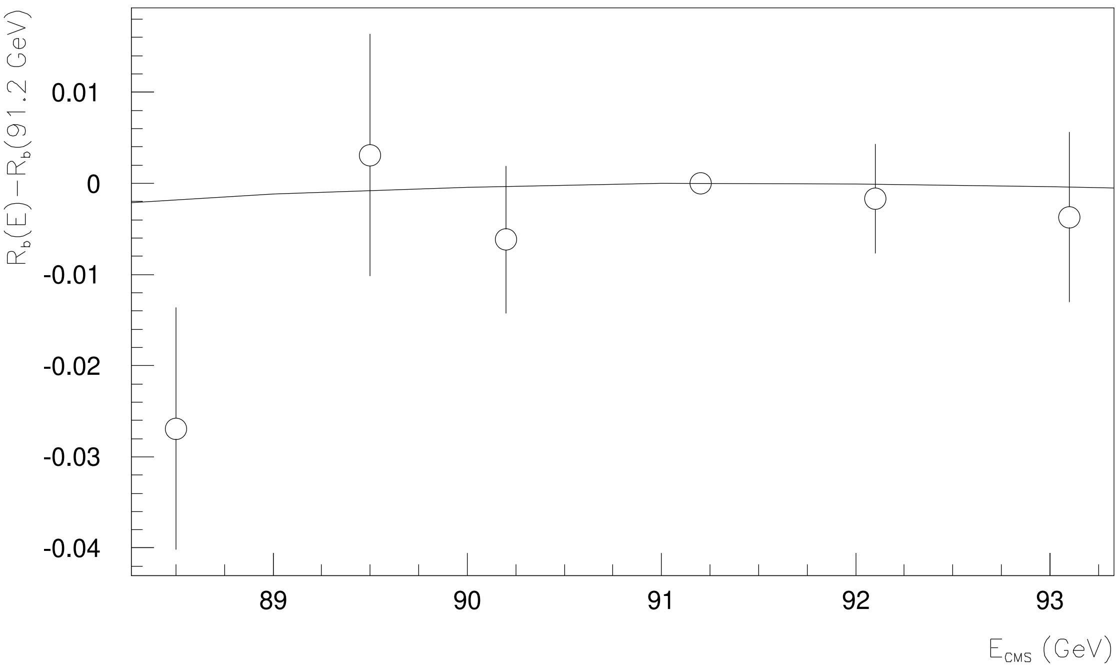

Figure 6: The difference $\Gamma_{b\bar{b}}\ /\Gamma_{had}(E_{CMS})$-$\Gamma_{b\bar{b}}\ /\Gamma_{had}(E_{CMS} = 91.2 \text{ GeV})$. The Standard Model prediction is shown by the curve.

4 Multivariate Analysis

This analysis is optimized to reduce the dependence on simulation as much as possible. A more detailed description of the method including some variants of the method presented can be found in [14].

4.1 Principle of the method

In this analysis the hadronic hemispheres were classified into three "flavours": *uds*, *c* and *b*. The *u*, *d* and *s* flavours were merged into a single *uds* light "flavour", since the tagging variables have very similar distributions for these three quark flavours.

4.1.1 Mathematical Formalism

The aim of the tagging algorithm is to classify hadronic events (separated in $N_F = 3$ flavours) into N_T tags or categories. Let C_I^l be the tagging probability (i.e. the tagging efficiency) of a hemisphere of flavour l into the category I ($I = 1, ..., N_T$ and $l = 1, ..., N_F$). The two dimensional array, C_I^l (hereafter called *classification matrix* $\tilde{C}$) is the same for both hemispheres. Except for very hard gluon emission, the quark and the antiquark are produced in opposite hemispheres so the same flavour should appear in both hemispheres.

The tensor of the observables $D_{IJ}, (I, J = 1, ..., N_T)$, is defined as the fraction of events tagged as I and J for hemispheres 1 and 2 respectively. It is multinomially distributed. If the hemispheres are independent, the expected fraction of events T_{IJ} can be written as

$$T_{IJ} = \sum_l C_I^l C_J^l R_l \qquad (I, J = 1, ..., N_T) \tag{11}$$

where R_l is the flavour fraction for a given sample. R_b is the branching ratio we want to extract.

The minimization of the objective function $G(C, R)$, defined as

$$G(C, R) = \sum_{IJ} \sum_{I'J'} (D_{IJ} - T_{IJ}) V^{-1} (D_{I'J'} - T_{I'J'}) \tag{12}$$

where V is the covariance matrix of the D_{IJ} elements, allows us to determine simultaneously the classification matrix $\tilde{C}$ and the composition of R_l.

The fit solution has to be compatible with the constraints: $\sum_l R_l = 1$, $\sum_I C_I^l = 1$ for all values of l. The method of Lagrange multipliers is appropriate to solve this problem [15]. The tensor itself has to obey the normalization condition $\sum_{IJ} D_{IJ} = 1$ with the optional requirement of symmetry $D_{IJ} = D_{JI}$.

V is a singular matrix due to the normalization condition. However, if one of the D_{IJ} elements is excluded, a new diagonal covariance matrix V^* can be defined [16] and the objective function is reformulated as

$$G(C, R) = \sum_{IJ} \frac{(D_{IJ} - T_{IJ})^2}{\sigma_{IJ}^2} \tag{13}$$

where the D_{IJ} elements are now considered independent with Poissonian errors, σ_{IJ}.

The problem cannot be solved if the number of observables (N_o) is less than the number of unknowns (N_u). We have for a given N_F and N_T, $N_o = N_T(N_T + 1)/2 - 1$, $N_u = N_T N_F - 1$. For example, for $N_F = 3$, N_T must be at least 6.

4.1.2 The Rotation Degeneracy

The solution of the above described fit is not uniquely defined since there is a degeneracy inherent in the tensor parameterisation. Let us introduce the set of vectors $\vec{V_I}$ whose three components are $(C_I^{uds}\sqrt{R_{uds}}, C_I^c\sqrt{R_c}, C_I^b\sqrt{R_b})$. Each tensor element T_{IJ} can be expressed as the scalar product $T_{IJ} = \vec{V_I} \cdot \vec{V_J}$. The scalar product is invariant under rotations in the space where the vectors $\vec{V_I}$ are defined. The vector $\vec{U}$ defined as

$$\vec{U} = \sum_I \vec{V}_I = (\sqrt{R_{uds}}, \sqrt{R_c}, \sqrt{R_b}) \tag{14}$$

can be interpreted as the composition vector of unit length. $\vec{U}$ and the set of $\vec{V}_I$ can be viewed as a rigid body. Once a particular solution has been found, other solutions may be generated by moving this rigid body according to three degrees of freedom; two degrees of freedom could be the position of the extremity of $\vec{U}$ on a sphere of unit radius, the third one an internal rotation around the $\vec{U}$ axis.

The degeneracy is removed in the b sector if two or more estimates of the C_I^b elements (hereafter denoted by X_I^b) are found. Let us define a modified objective function $G'(C, R)$ in which the estimates X_I^b are introduced

$$G'(C, R) = G(C, R) \ + \ \sum_I \frac{(C_I^b - X_I^b)^2}{\sigma_I^2} \tag{15}$$

where C_I^b are the same $\tilde{C}$ matrix elements as in function $G(C, R)$ and I only runs over the X_I^b considered. The σ_I are errors on the X_I^b estimates. The remaining degeneracy in the other sector can be removed, for instance, by fixing R_c to the Standard Model value. This constraint has no effect on any parameter of the b sector.

4.2 Hemisphere Tagging

The tagging algorithm can be viewed as a technique to distribute the events with different flavours in a set of hemisphere categories. Multidimensional analysis has been chosen to provide a more efficient separation than a cumulative set of cuts. The details of the technique can be found in [17,18].

4.2.1 Vertex Reconstruction of Hemispheres

Each event was subdivided into two hemispheres according to the sphericity axis. The particles were grouped in jets using the JETSET algorithm (LUCLUS) [6] with $d_{join} = 2.5$ GeV and the jet direction was given by the jet thrust axis. All particles assigned to jets making an angle of less than 90^0 with the sphericity axis were attributed to hemisphere one, the others to hemisphere two. In order to decrease correlations between opposite hemispheres, a primary vertex was computed on each side with an iterative procedure which includes all the charged particles of the hemisphere. If the fit probability of the resulting χ^2 was less than 0.05 the particle which contributes the largest value to the χ^2 was removed, and a new vertex fit was attempted. The process continued until a probability greater than 0.05 was obtained or only two particles remain.

The beam spot position and dimensions were measured fill-by-fill. This information was used as a constraint in the vertex fit on both sides. The average horizontal rms beam spot size was around 150μm [‡]. The vertical size was less than 50μm. The inclusion of this constraint increases the discriminating power of the tagging, but it represented a common feature of the hemispheres. The inclusion of the beam spot constraint did not seriously correlate the hemispheres.

4.2.2 Description of the Variables and Tags

The multidimensional analysis was based on a set of 12 discriminant variables per hemisphere. One variable (boosted sphericity) was computed with momenta only, the

[‡]However, a size of 200μm on average was introduced as a constraint in the fit.

remainder used the reconstructed particle trajectories near the interaction point. Three of them were connected to the χ^2 fit of vertices associated with various sets of particles. Three were distances between candidate secondary vertices and the primary vertex, and were sensitive to decay lengths. Three variables were different counters of secondary particles, and finally two variables were estimates of the total energy and P_t^2 associated with secondary particles. A full description of these cuts and variables can be found in [18].

The probabilities p_q, p_c and p_b of observing the 12 values of the variables for each hemisphere of an event were computed from model distributions taken from simulation. The logarithm of these three probabilities, called hereafter "class-likelihoods" ($L_q = \ln\ p_q$, $L_c = \ln\ p_c$ and $L_b = \ln\ p_b$), were the basis of the classification.

The hemispheres were first classified by 3 tags as follows. The flavour likelihoods were sorted in decreasing order as L_{first}, L_{second}, L_{third}. The hemisphere was tagged uds, c or b according to the highest probability, L_{first}. In order to define the six categories mentioned in section 4.1.1, we introduce the concept of a "winning margin"

$$\Delta = ln(p_{first}/p_{second}) \ = \ L_{first} - L_{second} \tag{16}$$

which is an indicator of tag clarity. Figure 7 shows the distributions of the "winning margin" observed in the simulation for the three tags. The c-tag (category 3) is less populated and poorly enriched. It has not been subdivided. The uds and b tags are afterwards subdivided into categories according to the following criteria:

- $uds - tight : \Delta > \Delta_q^{cut}$ (category 1)
- $uds - loose : \Delta < \Delta_q^{cut}$ (category 2)
- $b - loose : \Delta < \Delta_b^{cut,low}$ (category 4)
- $b - medium : \Delta_b^{cut,low} < \Delta < \Delta_b^{cut,high}$ (category 5)
- $b - tight : \Delta > \Delta_b^{cut,high}$ (category 6)

The values of the cuts were $\Delta_q^{cut} = 2.0$, $\Delta_b^{cut,low} = 3.0$ and $\Delta_b^{cut,high} = 6.0$. They are chosen in order to have similar population in the categories.

4.2.3 Simulation Results

This overview of the tagging performances – estimated from 450000 simulated events generated with a b lifetime of 1.6 ps – is necessary to understand the assumptions that will be made to solve the degeneracy problem. The simulated events were generated using DELSIM [7] and processed through the same analysis chain as the data:

- Figure 8 shows the purity and the efficiency of the single hemisphere b tag as a function of the purification cut $\delta = \Delta_b^{cut,high}$. The purity and efficiency of the double hemisphere b tag are also given, when the same $\Delta > \Delta_b^{cut,high}$ cut on Δ is applied to both sides. Without any Δ cut, the double tag purity is already 84% and rapidly approaches 100% when the cut is applied at the cost of a low efficiency. In practice, the D_{66} component of the tensor with a cut on Δ at 6.0 corresponds to almost pure b events.
- The lego plot of fig. 9 shows for the simulation the population of the double tagged categories which is the input of the fit (the population for data shows the same features). The contributions of the three flavours are also detailed there. As can be seen uds and b events populate opposite corners, while the c events overlap with uds and b.

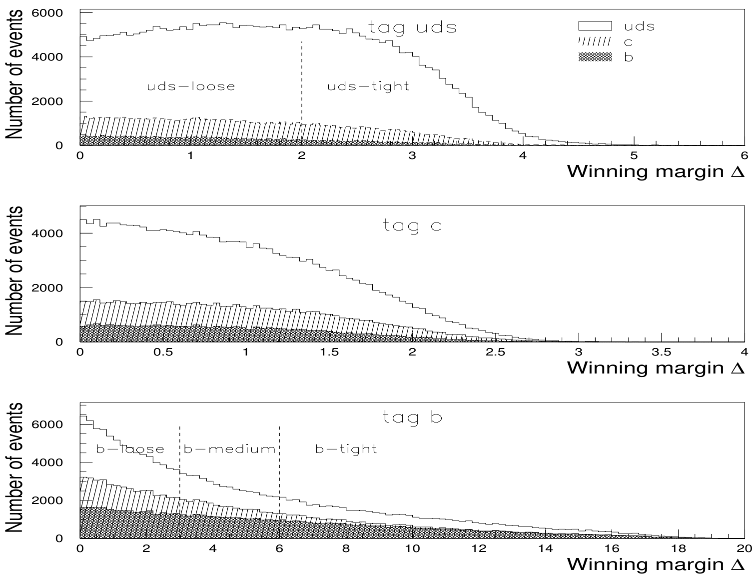

Figure 7: Distributions obtained from the simulation of the winning margin Δ in the uds, c and b hemisphere tag. The filled areas show the different heavy flavour contributions to the events in a given tag. The dashed lines show the cuts to separate the 6 different categories.

4.3 $\Gamma_{b\bar{b}}/\Gamma_{had}$ Measurement

An interesting feature of independent hemisphere tagging is that full b purity can be approached in one hemisphere by imposing large values of the clear winning cut δ in the opposite one. This good separation is only present for b quarks. The set of estimates X_I^b can then be obtained from the asymptotic purities.

Among the events which have been tagged as a b in one hemisphere with a winning margin $\Delta > \delta$, consider the number, N_I, of events classified in category I for the other hemisphere and the fraction

$$f_I(\delta) = \frac{N_I(\delta)}{\sum_J N_J(\delta)} = \sum_l C_I^l R_l'(\delta) \tag{17}$$

where $R_l'(\delta)$ denotes the composition of the sample purified by the δ cut. When the clear winning cut, δ, increases and if the hemispheres are independent, $f_I(\delta)$ tends to C_I^b. Formally

$$X_I^b = \lim_{\delta\to\infty} f_I(\delta) = C_I^b \tag{18}$$

since R_{uds}', R_c' and R_b' tend to 0, 0 and 1 respectively, due to the fact that increasing δ results in samples with higher b purity, as can be seen from fig. 7. It should be noted that in eqn. 17 the contents of nearby bins are highly correlated. For this reason, in order to extract C_I^b and to evaluate the statistical errors, we define the uncorrelated ratio $f_I^{uncorr}(\delta)$:

$$f_I^{uncorr}(\delta_i) = \frac{N_I(\delta_i) - N_I(\delta_{i+1})}{\sum_J [N_J(\delta_i) - N_J(\delta_{i+1})]} \tag{19}$$

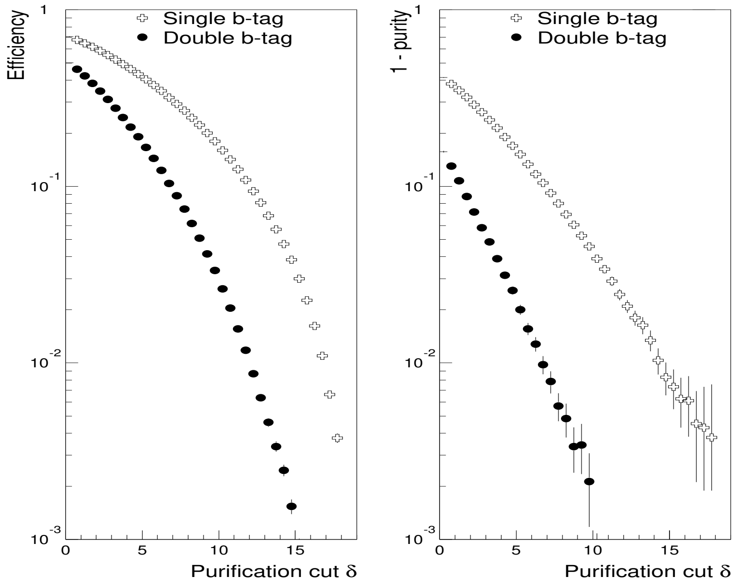

Figure 8: Efficiency and purity of the single and double hemisphere b tags versus the value of the clear winning cut $\delta = \Delta_b^{cut}$ for simulated events. The purity is plotted in the form 1 – purity.

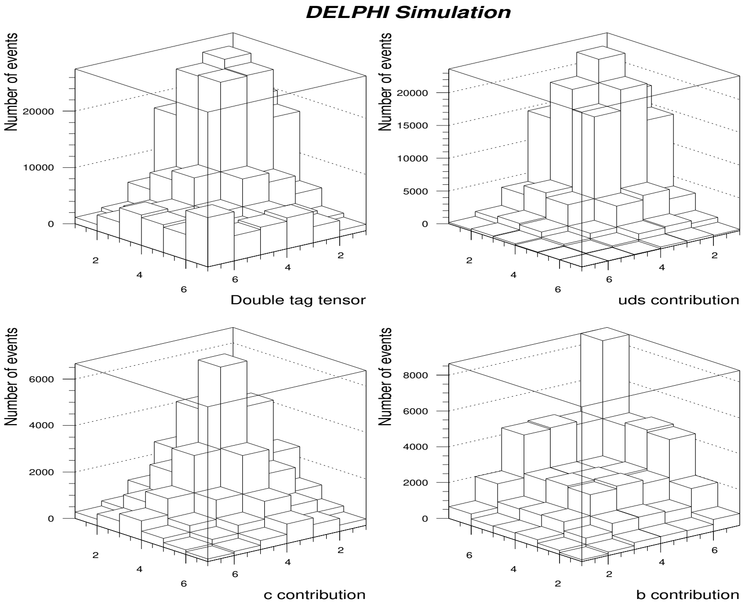

Figure 9: Population of the double tag tensor with their uds, c and b contributions for simulated events. Note that the axes for the b contribution are rotated by 180 degrees with respect to the other plots.

which reaches the same limit as $f_I(\delta)$ for large values of δ. Index i represents the number of bin.

Different parameterisations of f_I have been tried to fit the asymptotic value: uniform in the last bins of the distribution, exponential, inverse polynomial functions, etc. However, it was found experimentally that the best parameterisation of our data is an exponential function convoluted with a Gaussian resolution function,

$$f_I^{uncorr}(\delta) = p_{I1} \ + \ \frac{p_{I2}}{\sqrt{2\pi}p_{I3}} e^{-p_{I4}\delta} e^{-\delta^2/2p_{I3}^2} \tag{20}$$

where the p_{Ii}, $i = 1, ..., 4$ are free parameters of the fit. Only the parameter p_{I1} has physical meaning; it gives the asymptotic value X_I^b. The plots of the f_I^{uncorr} distributions for the simulation and data as a function of the clear winning cut value, δ, are shown in figs. 10 and 11 respectively. For simulation, good agreement can be seen between the asymptotic limit and the expected C_I^b matrix element. The validity of the asymptotic fit assumption, that there is no irreducible background from light and c quarks, can be clearly seen in fig. 10.

Introducing the estimates X_I^b, we have minimized the function $G'(C, R)$ fixing the R_c parameter to the measured value of 0.171 ± 0.014 [1]. As has already been noted in section 4.1.2, fixing this parameter (to an arbitrary value) has no effect on any parameter of the b sector. Table 5 compares the C_I^b values obtained from the minimization with the X_I^b estimates and with their expected values. Good agreement can be seen between the three sets of numbers. To some extent, the agreement between C_I^b and X_I^b is due to the fact that X_I^b is used in the estimation of C_I^b. The fitted b fraction for the simulated sample (after accounting for acceptance losses, see section 4.4.3) was found to be $R_b = 0.2174 \pm 0.0042$, to be compared with the generated value of 0.217.

	Simulation			*Data*	
C_I^b Matrix elements	*Expected values of* C_I^b	*Asymptotic values* X_I^b	*Fitted values of* C_I^b	*Asymptotic values* X_I^b	*Fitted values of* C_I^b
C_1^b	0.0307	0.0290(20)	0.0305(19)	0.0172(19)	0.0178(18)
C_2^b	0.0838	0.0853(29)	0.0855(19)	0.0756(43)	0.0770(36)
C_3^b	0.1805	0.1768(55)	0.1804(32)	0.1486(43)	0.1468(26)
C_4^b	0.1825	0.1800(30)	0.1796(19)	0.2126(28)	0.2125(22)
C_5^b	0.1758	0.1744(41)	0.1752(20)	0.2026(43)	0.2082(24)
C_6^b	0.3467	0.3489(45)	0.3487(36)	0.3393(71)	0.3378(42)

Table 5: X_I^b parameters from asymptotic behaviour and the corresponding C_I^b fitted values with the objective function G', for simulated and real data sets. Comparison with the expected value for simulation. The errors are on the last two digits and are given in brackets.

For the real data sample, the values of C_I^b are in agreement with the X_I^bs. The fitted b fraction after accounting for acceptance losses is in this case

$$R_b = 0.2245 \pm 0.0063 \tag{21}$$

with $G'/ndf = 14.1/9$. The minimum of $G'(C, R)/ndf$ is very similar to that of the $G(C, R)/ndf$ function. This means that the X_I^b introduced in the objective function are

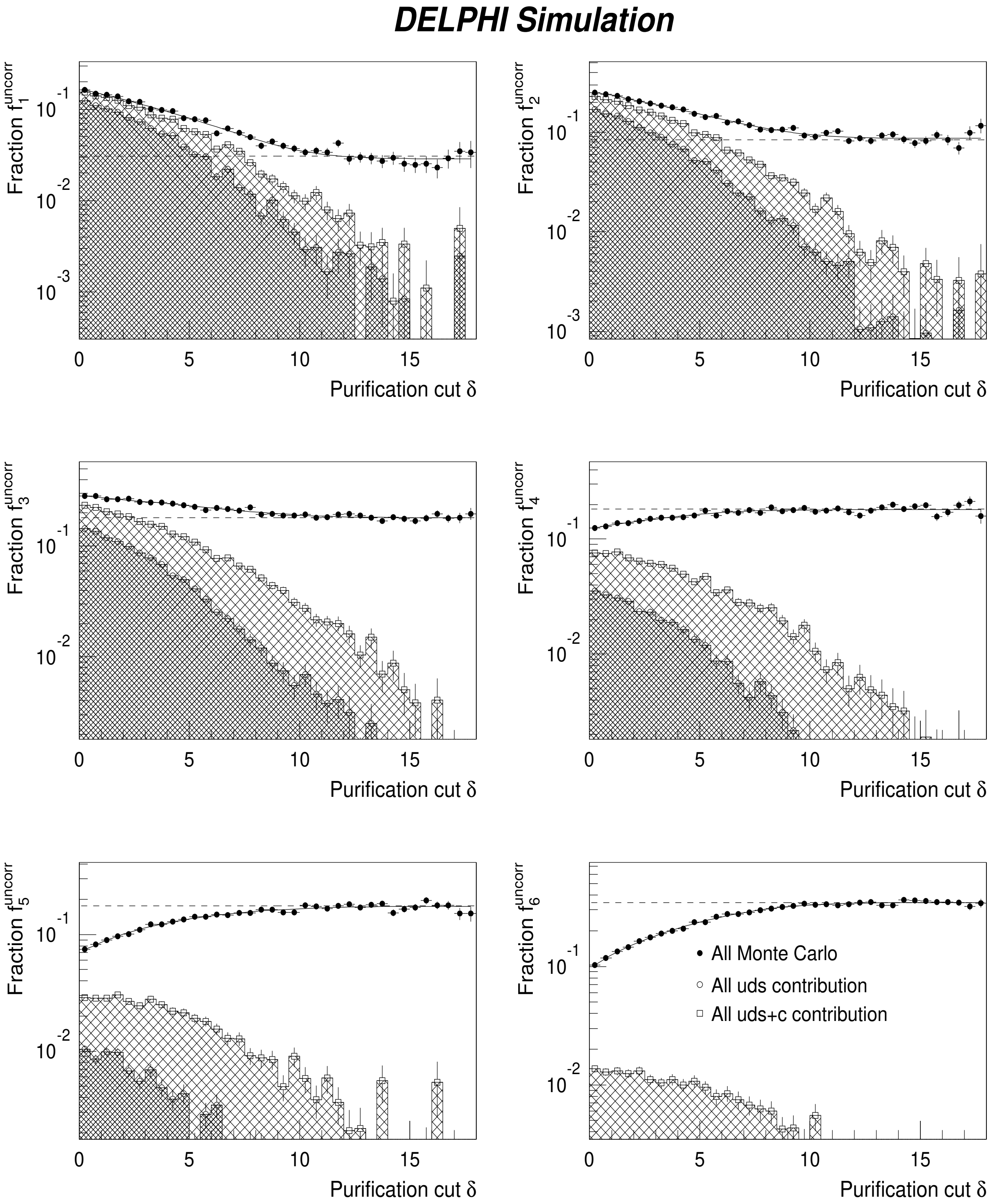

Figure 10: $f_I^{uncorr}(\delta)$ distributions with their asymptotic fits (see text) for simulation. If hemispheres are independent, $f_I^{uncorr}(\delta)$ should tend asymptotically to C_I^b when δ increases. The big cross-hatched area indicates the c contamination while the small cross-hatched area is the uds contribution. No asymptotical irreducible uds and c background is observed in the asymptotic region, particularly in f_4, f_5 and f_6 distributions which are the most significant for the extraction of R_b. The dashed horizontal lines show the true values for C_I^b.

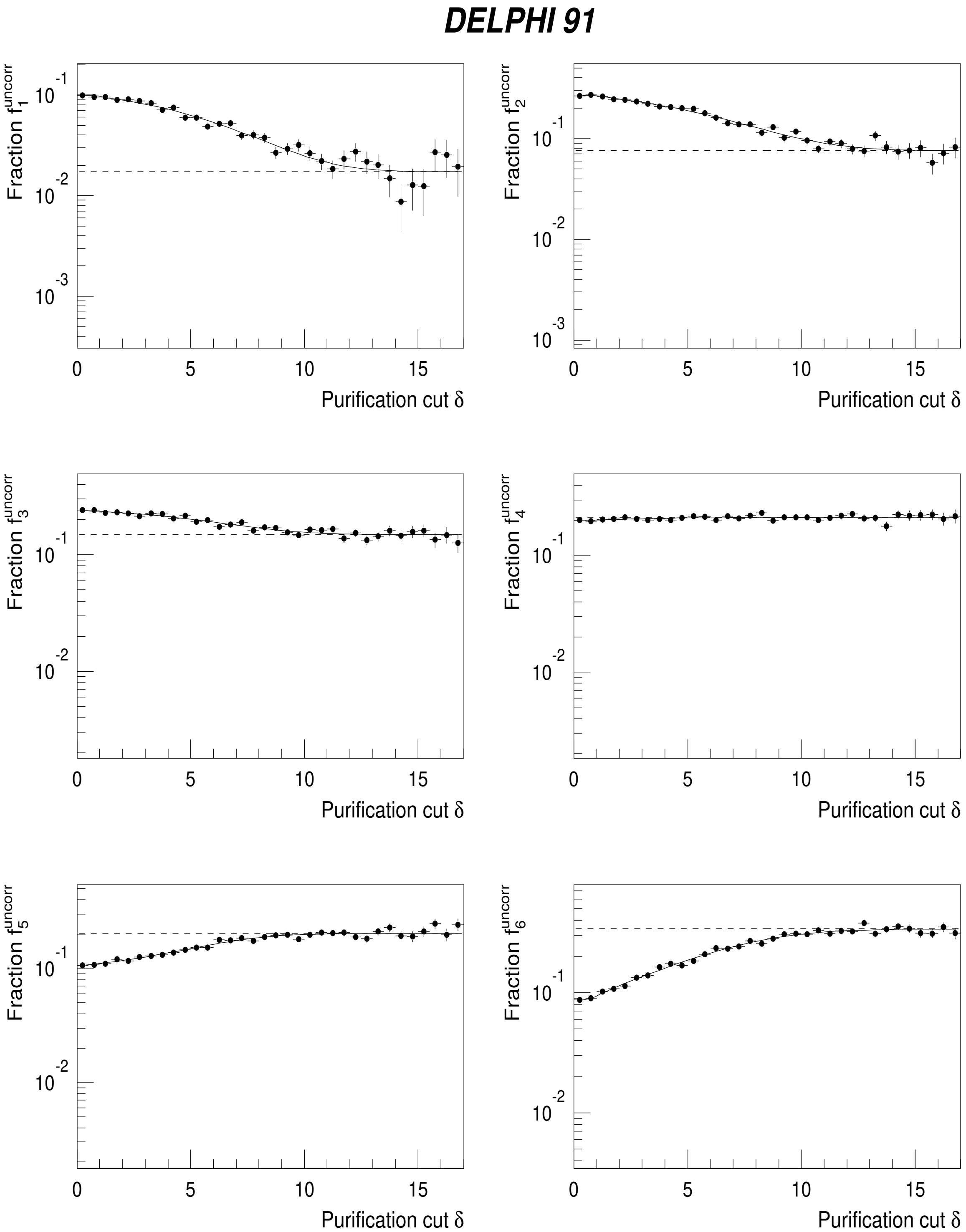

Figure 11: $f_I^{uncorr}(\delta)$ distributions with their asymptotic fits for DELPHI data. The dashed horizontal lines show the asymptotic values of X_I^b.

compatible with the set of degenerate solutions of the tensor fit alone. If another set of estimators X_I^b is used the minimum of $G'(C,R)$ increases much more. For example, with the X_I^b taken from simulation, G'/ndf doubles.

4.4 Determination of Systematic Errors

The systematic errors have been determined separately for different sources. Only the most relevant ones are described in the following.

4.4.1 Hemisphere Correlation and C^b Asymptotic Estimation

To allow for hemisphere correlations, the expressions for T_{IJ} in the function $G'(C,R)$ are replaced by

$$T_{IJ} = \sum_l C_I^l C_J^l (1 + \rho_{JI}^l) R_l \tag{22}$$

where the double tag hemisphere correlation factor for a given flavour, l, is defined as

$$\rho_{JI}^l = \frac{D_{IJ}^l}{C_I^l C_J^l} - 1, \tag{23}$$

D_{IJ}^l being the double tag efficiency. As before, the index I refers to the first hemisphere tag and J to the tag for the second. The correlation factors are predicted from the simulation and are shown in fig. 12, with statistical errors, for the six categories. Most of these factors are small or negligible for the determination of R_b [§].

Correlations are also relevant for the asymptotic estimation of C_I^b, so that eqn. 18 is replaced by

$$\lim_{\delta\to\infty} f_I(\delta) = \left\{ 1 + \lim_{\delta\to\infty} \rho_{I6}^b(\delta) \right\} C_I^b \tag{24}$$

The main correlation factor for the R_b measurement is ρ_{66}^b. Figure 13 shows the variation of this coefficient with δ for simulation. It has no dramatic behaviour at large values of δ and for the standard cut is $\rho_{66}^b = 0.018 \pm 0.010$, where the error is due to the limited Monte Carlo statistics.

As a cross check, it is interesting to study how much R_b changes when using eqns. 22 and 24 (where the $\lim_{\delta\to\infty} \rho_{I6}^b(\delta)$ has been approximated by $\rho_{I6}^b(6.0)$) assuming the hemisphere correlations shown in fig. 12 from the simulation, instead of eqns. 11 and 18. R_b varies by less than 1 %, 0.5 standard deviation of the statistical error on simulation (0.0042). Moreover, asymptotic correlation factors were changed taking into account the small instabilities on $\rho_{I6}^b(\delta)$ resulting from changes in δ. A negligible change on the fitted R_b value was found.

In the absence of hemisphere correlations the R_b measurement is simulation independent (the significance analysis takes background efficiencies from simulation whereas in this analysis they are extracted directly from the data). However, in the presence of small correlations, model uncertainties may change R_b. Therefore we have checked whether the correlation effects, in the matrix and asymptotic terms of the G function, depend on these uncertainties, using the same simulated sample re-weighted to different physical parameters (in order to minimize the statistical fluctuations).

[§] For example, the largest factor is $\rho_{11}^b = 0.52 \pm 0.15$, but it affects only 1/1000 of $b\bar{b}$ events.

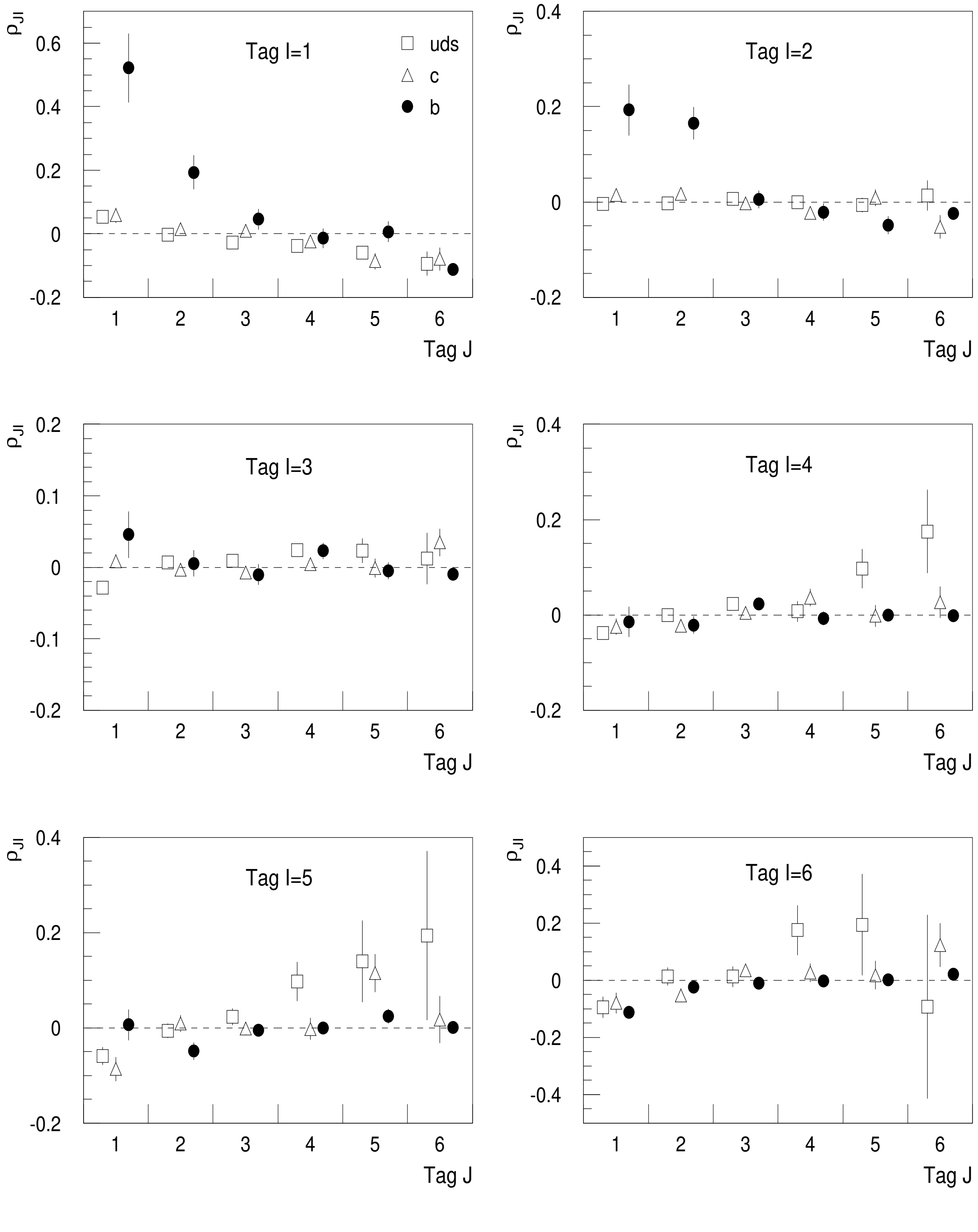

Figure 12: Double tag hemisphere correlation factors ρ^l_{JI} for simulation.

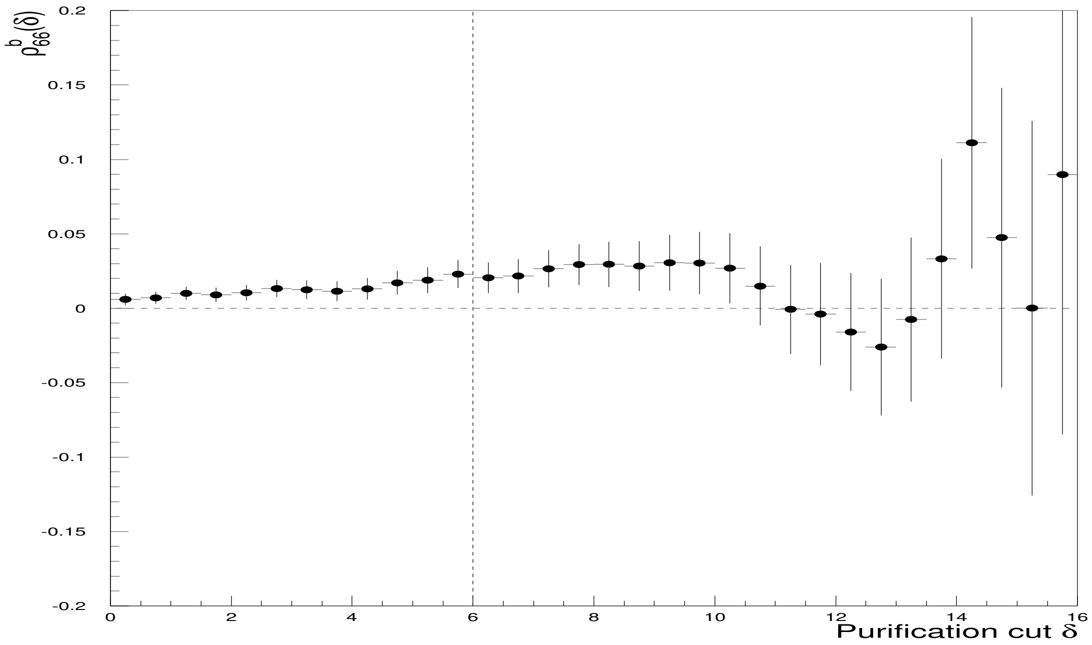

Figure 13: Double tag hemisphere correlation factor ($I = 6, J = 6$), as a function of δ. For the standard cut at $\delta = 6$, the value of ρ^b_{66} is 0.018 ± 0.010 and it remains rather stable over the whole range. Note that, by definition of ρ^b_{66}, the points are bin-to-bin correlated.

The change in R_b was 0.0004 when the b lifetime changed from 1.6 ps to 1.2 ps. Taking into account the current uncertainty on τ_b (± 0.034 ps [12]) this leads to a contribution of less than 0.0001 on R_b. The effect due to the b fragmentation function was estimated by varying the mean energy of B hadrons by $\pm 3\%$ and a change of 0.0004 was found on R_b.

The effect of hard gluon emission producing a $b\bar{b}$ pair in the same hemisphere (about 2 % of the $b\bar{b}$ events according to the simulation) might be the source of an excess of b events in the (small I,large J) and (large I,small J) cells. However, the distributions of the tagging variables in "double b" hemispheres are, in the simulation, practically the same as in an ordinary b hemisphere (the B hadrons have a smaller energy, so that the b character is not enhanced). This explains why there is no special accumulation of such hemispheres at large values of δ, producing negative correlations in the C^b_I estimates for large I and corresponding positive correlation for low I. Actually there is a small, but statistically significant depletion in the (1,6) bin of fig. 12. This suggests a cancellation with a correlation of opposite sign, maybe between the tagging variables. In order to evaluate systematic errors, we have performed a fit on the simulated data sample, removing the events with two b jets in the same hemisphere and recomputing the b fraction in the reduced sample. The difference between the fitted value of R_b and the expected one is 0.0021. As in section 3.3, 20% of this number was taken as systematic uncertainty.

The beam spot constraint can be a source of correlations since the beam size is common for both hemispheres. A 10% uncertainty was assumed (which corresponds to the accuracy of the size determination) and a variation on R_b of 0.0005 was found.

The relative production rate of $D^{\pm}$ and D^0 can be a source of correlations because the lifetime of these two mesons differ. The relative production rate was varied by 20% [9] and a change on R_b of 0.0005 was obtained. The lifetimes of D hadrons were varied according to [9] and R_b changed by 0.0002. The uncertainty due to charm decay multiplicity was estimated as in the significance analysis and a value of 0.0003 was found. The effect due to the charm fragmentation function was estimated by varying the mean energy of D hadrons by $\pm 4\%$ and a change of 0.0003 was found on R_b. Potential errors from the light quark sector (due to the production rate of long-lived particles and secondary interactions) were estimated as in the significance analysis and a negligible change on R_b was found.

The sum of all these effects is found to be less than 0.5 %. This shows that the method is almost insensitive to the uncertainties on the physical parameters.

The stability of the asymptotic estimation of C^b was tested using alternative f_I parameterisation functions, as described in 4.3. The R_b values obtained by minimizing the $G'(C,R)$ objective function show a dispersion (for the different parameterisations used) of 1 %.

The systematic error due to correlation effects (including contributions of the C^b asymptotic estimation) was assumed to be well described in the simulation within the statistical error (0.0042), which can be taken as a conservative evaluation of the systematic error on R_b. Adding this error in quadrature to the uncertainty from hard gluon emission, the total systematic error does not change within the given accuracy. Moreover, we use the difference between fitted and expected R_b on simulation (0.0004), as a correction to be applied to the R_b fitted with the data.

As a check on the correlation due to the limited VD acceptance, the cut on $|\cos\Theta_{thr}|$ was changed from 0.65 to 0.85. No significant change was observed on R_b.

4.4.2 Effect of Tagging and Modelling

Two training samples have been used to compute the *"class-likelihoods"* of section 4.2.2 (with different lifetimes 1.2 and 1.6 ps, and different versions of the simulation program). We have found a difference of 0.0007 on R_b. Another effect to be considered is the choice of $\Delta_b^{cut,low}$ and $\Delta_b^{cut,high}$ which define the boundaries of b categories. A change in the boundaries modifies the C_4^b, C_5^b and C_6^b values, but $C(b,b) = C_4^b + C_5^b + C_6^b$ and the compositions (in particular R_b) should remain constant. The spread of values gives a contribution to the systematic error of 0.0009. In principle the method is insensitive to tagging and modelling effects, but nevertheless we conservatively add these contributions.

4.4.3 Other Errors

- *Acceptance correction.* This contribution is mainly due to the selection criteria for hadronic Z events. JETSET events were generated with $\Gamma_{b\bar{b}}/\Gamma_{had}$ of 0.217. After acceptance cuts, this value is modified to 0.2211 ± 0.0007. This induces an acceptance correction of $(1.9 \pm 0.3)\%$.
- *Dependence on* $\Gamma_{c\bar{c}}/\Gamma_{had}$. We refer here to the actual number of charm events, which should be distinguished from R_c in the fit. When changing the $c\bar{c}$ fraction by $\pm$ one standard deviation of its measured value ($R_c = 0.171 \pm 0.014$ [1]) in the fit to the simulation, we found a variation of $\mp$ 0.0012 on R_b.

Table 6 summarizes the sources of systematic error and their contributions to the error on $\Gamma_{b\bar{b}}/\Gamma_{had}$.

Therefore we quote as final value, including acceptance and systematic corrections,

$$R_b = 0.2241 \pm 0.0063(stat.) \pm 0.0046(syst.). \tag{25}$$

This value averages the 7 different centre-of-mass energies around the Z peak. However, the small change in the R_b value for the different points is negligible with respect to the statistical uncertainty.

5 Combination of the Methods

To combine the two measurements the statistical correlation has been measured by applying both methods to six independent simulated event samples, yielding a correlation of 11% with large uncertainties. The corresponding 90% C.L. upper limit gives a correlation of 60%. Conservatively, a 60% correlation between the statistical errors has been used when combining the two results.

The errors due to hemisphere correlation, $\Gamma_{c\bar{c}}$ and acceptance bias, have been taken as fully correlated between the two analyses. Table 6 summarizes the systematic errors for both analyses.

Source of systematics	Significance Analysis	Multivariate Analysis
Hemisphere Correlation	0.0031	0.0042
$Br(Z \to bb)$ acceptance bias	0.0010	0.0007
Light quark efficiency	0.0020	
Charm efficiency	0.0021	
Effect of tagging and modelling		0.0011
$\Gamma_{c\bar{c}}$	0.0019	0.0012
Total	0.0048	0.0046

Table 6: Systematic errors in the two analyses. Errors on the same line of the table (excluding the total) have been assumed to be fully correlated.

As our final result we find

$$R_b \;=\; 0.2209 \;\pm\; 0.0041\,(stat.) \;\pm\; 0.0042\,(syst.) \;\pm\; 0.0018\,(\Gamma_{c\bar{c}}).$$

This value agrees well with those measured by other experiments [3,19] and with that predicted by the Standard Model [2]. The current precision is not sufficient to constrain the Standard Model parameters. However with the analysis of more data and a tighter event selection, the decrease of statistical and systematic errors is expected and constraints on the top quark mass will be possible.

Acknowledgements

We are greatly indebted to our technical collaborators and to the funding agencies for their support in building and operating the DELPHI detector, and to the members of the CERN-SL Division for the excellent performance of the LEP collider.

References

[1] The LEP Collaborations, *Updated Parameters of the Z Resonance from Combined Preliminary Data of the LEP Experiments*, CERN-PPE/93-157.

[2] W. Hollik, Fortsch.Phys. 38 (1990) 165.

[3] D. Buskulic *et al.* (ALEPH collaboration), Phys. Lett. **B313** (1993) 535.

[4] P. Aarnio *et al.* (DELPHI Collaboration), NIM **A303** (1991) 233-276.

[5] P.Abreu *et al.* (DELPHI Collaboration), Nucl. Phys. **B** 417 (1994) 3-57.

[6] T.Sjöstrand, Comp. Phys. Comm. **39** (1986) 347;
T.Sjöstrand and M.Bengtsson, Comp. Phys. Comm. **43** (1987) 367;
T.Sjöstrand: JETSET 7.3 manual, preprint CERN-TH 6488/92 (1992).

[7] DELSIM Reference Manual, DELPHI 87-98, Geneva, 1989.

[8] P.Abreu *et al.* (DELPHI collaboration), Phys. Lett. **B312** (1993) 253;
O. Adriani *et al.* (L3 Collaboration), Phys. Lett. **B317** (1993) 474.

[9] K.Hikasa *et al.* (Particle Data Group), Phys. Rev. **D45** (1992) 1.

[10] D. Coffman *et al.* (MARK III Collaboration), Phys.Lett. **B263** (1991) 135.

[11] P.Abreu *et al.* (DELPHI Collaboration), Z. Phys. **C59** (1993) 533.

[12] W. Venus, *b Weak Interaction Physics in High Energy Experiments*, Proc. Conf. on Lepton Photon Int., Cornell (1993) 274.

[13] D.Bardin *et al.*, CERN-TH 6443/92.

[14] P. Billoir *et al.*, *Measurement of the* $\Gamma_{b\bar{b}}/\Gamma_{had}$ *branching ratio of the Z by hemisphere double tagging with minimal Monte Carlo dependence*, Univ. Valencia preprint IFIC/94-23.

[15] NAGLIB Manual. CERN Program Library.

[16] A.G. Frodesen, O. Skjeggestad, H. Tofte, *Probability and Statistics in Particle Physics*, Universitetsforlaget 1979.

[17] Ch. de la Vaissiere and S.Palma-Lopes in the AIP Heavy Flavour workshop proceedings (1989) p440.

[18] P. Billoir *et al.*, *B-tagging by hemispheres: description of variables and results on Monte Carlo*, LPNHE 94-05.

[19] O. Adriani *et al.* (L3 collaboration), Phys. Lett. **B307** (1993) 237;
R. Akers *et al.* (OPAL collaboration), Z. Phys. **C61** (1994) 357;
R. Akers *et al.* (OPAL collaboration), CERN-PPE/94-106.